

pubs.acs.org/acsaom Article

Accidental BICs and Chiroptical Response of Hollow Channels in Silicon Nanodisk Resonator-Based Metasurfaces for Chiral Sensing

Shubhanshi Sharma,* Alina Karabchevsky, and Shailendra K. Varshney



Cite This: ACS Appl. Opt. Mater. 2025, 3, 364-374



Read Online

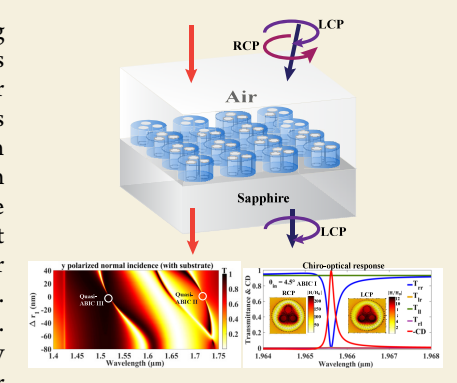
ACCESS

Metrics & More

Article Recommendations

Supporting Information

ABSTRACT: Achieving light confinement at the nanoscale is essential for enhancing light-matter interactions, and bound states in the continuum (BICs) have emerged as promising approaches. This study presents a dielectric metasurface design featuring air channels within a silicon nanodisk resonator, demonstrating symmetry-protected BICs (SPBICs) and accidental BICs (ABICs). Here, we report SPBICs that exhibit an exceptionally high quality (Q) factor at very low asymmetry parameters. An increase in the asymmetry decreases the Q-factor quadratically. To alleviate this, we observe that the SPBIC can be transformed into ABICs by adjusting the radius of one air channel that converts the resonances from quasi-SPBICs to quasi-ABICs. Introducing a third air channel with an optimized radius helps to achieve an ultrahigh Q-factor ≈ 38000 . Multiple ABICs with enhanced local fields were observed for both x- and y-polarizations. The triple air channel design also achieves a maximal extrinsic chiral response by breaking the symmetry through an oblique incidence angle, which influences circular



dichroism (CD) and transmittance for different circular polarizations. Numerical simulations reveal that the proposed chiral metasurface achieves a near-perfect value of CD = -0.99, a Q-factor of 8846, and a field enhancement by a factor of 200. Moreover, slightly tilting the nanodisk can realize a high intrinsic chirality (CD = -0.88) with a Q-factor $\approx 10^4$. The concept of chiral BICs studied here can be utilized in, but not limited to, applications such as chiral sensing, bioimaging, and chiroptical spectroscopy.

KEYWORDS: accidental bound states in the continuum, chiral metasurfaces, dielectric metasurfaces, fano resonances, circular dichroism

1. INTRODUCTION

The ability to manipulate light-matter interactions at the nanoscale, mainly by controlling amplitude, polarization, and phase, ^{1,2} is crucial for advancing optical technologies³ that span a wide range of fundamental sciences. ⁴ Exploring bound states in the continuum (BIC) enhances field confinement at the nanoscale. ⁵ The BICs are localized, nonradiative electromagnetic states that exist within the radiation continuum, theoretically resulting in an infinite quality factor (Q) and zero resonance line width. ^{5,6} As a result, they are not detectable in the resonance spectrum unless a symmetry operation is performed. The BICs are generally classified into symmetry-protected BICs (SPBICs) and accidental BICs (ABICs).

The symmetry-protected BICs arise from the preservation of geometrical symmetry with respect to the incident light. ^{7–9} In contrast, accidental BICs occur when all leakage channels have vanished for a specific wavevector in k-space or a particular geometric parameter. ^{10–12} Both SPBICs and ABICs can be converted into quasi-bound states in the continuum (QBICs) by perturbing the structure, giving rise to either Fano or electromagnetically induced transparency (EIT) resonances or both in the spectrum, with a finite and high *Q*-factor. ¹³

Due to the complexity of introducing an optimum asymmetry, achieving symmetry-protected quasi-BICs (SPQBICs) remains a significant challenge. However,

accidental quasi-BICs (AQBICs) are easier to achieve, as they allow for simpler structural designs that are less dependent on symmetry and are more practical for fabrication. The BICs have been demonstrated in various photonic structures, including photonic crystal slabs, ^{14,15} metamaterials, ¹⁶ plasmonic structures, ^{17,18} hybrid plasmonic-dielectric structures, ^{19,20} compound waveguide grating structures ^{21,22} and hybrid waveguide meta structures. ²³ These structures are used to enhance various physical processes such as nonlinearity, ^{24,25} chirality, ^{26,27} sensing, ^{28,29} and photon emission. ^{30,31} It will be noteworthy to combine BICs with chirality, which has tremendous potential to attain maximum optical chirality.

Chirality is a common phenomenon in nature where an object cannot match its mirror image through symmetry operations such as rotation or translation. It has significant importance across various fields, including optics and photonics, 32,33 material sciences, 34,35 biomedicine, 36,37 and

Received: November 25, 2024
Revised: January 8, 2025
Accepted: January 13, 2025
Published: January 21, 2025





drug development. 38,39 Optical chirality arises when a chiral object interacts with the light of a specific helicity while being transparent to the light of the opposite helicity due to variations in amplitude, phase, and polarization. The key measures of optical chirality include circular dichroism (CD), optical rotation, and a change in transmission. In natural materials, chirality is typically weak. Therefore, the chiroptical response is enhanced by geometrically induced chiral structures, often referred to as intrinsic or extrinsic chirality. A few examples of intrinsically chiral structures are shown, viz. photonic crystals, metamaterials, origami-based metamaterials, three-dimensional nanostructures, and two-dimensional materials, whereas extrinsic chirality can be achieved by changing the incident angle in achiral structures. 40-42 Combining BICs and chirality generates chiral quasi-BIC metasurfaces with improved circular dichroism for intrinsic and extrinsic chirality which can be utilized in applications such as but not limited to, linear and nonlinear chiral sensing, chiral imaging, enantiomer separation, and chiral quick response (QR) codes. 43-47 Recently, different designs such as notched nanoresonator metasurfaces, 48,49 tilted trapezoidal photonic crystal slabs, 50 air channel embedded nanoresonator metasurfaces, 51,52 height asymmetric metasurfaces,⁵³ and waveguide grating⁵⁴ have been proposed to achieve near perfect intrinsic and extrinsic chirality.

However, designs reported in the literature are mainly driven by SPBIC, where asymmetry plays a significant role. It is known that the Q-factor decreases with an increase in the asymmetry parameter. In order to achieve a high Q-factor, the asymmetry parameter should be relatively small, which may pose challenges in the fabrication. Also, it is noteworthy that the previously mentioned designs lack multiple chiral responses. In this work, we report two simpler designs of metasurfaces, namely, (i) nanodisk with two air channels depicting the SPBICs with a moderate Q-factor and (ii) nanodisk with three air channels where the SPBICs are transformed into AQBICs possessing a high Q-factor. The multiple accidental BICs with a high Q-factor are generated for linearly polarized incident light, extrinsic, and intrinsic chiroptical response. The BICs characteristics of the nanodisk resonators with two and three air channels are analyzed through numerical simulations. In the case of the two air channel design, we achieve high-quality factor multiple SPQBICs, with a magnetic dipole, toroidal electric dipole, and quadrupole moments as their primary moments when the air channels are displaced from the center to induce asymmetry. A small value in the asymmetry parameter in the presence of the substrate yields a field enhancement of $\approx 10^3$ and a Q-factor of 10⁵ in the dominant mode of the magnetic dipole moment. On the other hand, a nanodisk with triple air channels could generate multiple accidental BICs for both x and y-polarized light. In the case of x-polarized light, AQBICs exhibit a high Q-factor of 38000 when all three air channels are of the same radius. Such a metasurface comprised of a nanodisk with three air channels demonstrates a multiresonant extrinsic chiral response for an oblique incidence with a maximum CD = -0.99 and a high Q-factor of 8846. Other than the extrinsic chirality, the structure can exhibit high intrinsic chirality (CD = -0.88) and a reasonably high Q factor on the order of four when the nanodisk resonators are tilted. The chiroptical response of the nanodisk exhibits the potential to be utilized in chiral sensing, separation of enantiomers, bioimaging, and chiroptical spectroscopy.

2. METASURFACE DESIGNS

The proposed planar metasurface on the x-y plane features an infinite array of periodic silicon nanodisk resonators arranged in a square lattice. The nanodisk resonators that constitute the metasurfaces have multiple air channels. The metasurface is defined by specific parameters: period $P_x = P_y$, nanodisk radius r_{out} height (or thickness) t, individual air-hole radius r_{in} , and separation between two consecutive air-holes g. The entire metasurface, composed of nanodisk resonators, is placed on a sapphire substrate, as illustrated in Figure 1a. We consider two

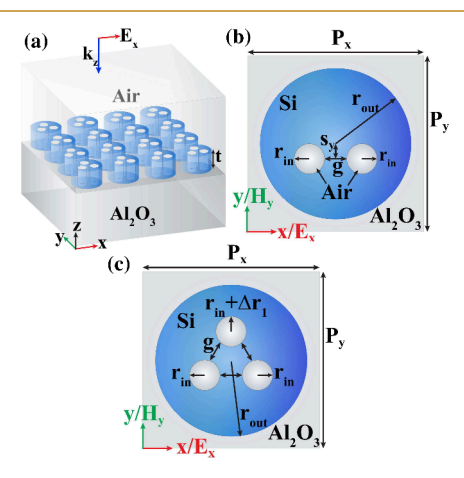


Figure 1. (a) Illustration of an infinite periodic array of the hollow-channel-aided silicon nanodisk resonator metasurface placed on the sapphire substrate. Top view of the unit cell of the nanodisk resonator with (b) two air channels offset in the negative *y*-direction and (c) three air channels placed on equilateral vertices.

independent nanodisk resonator designs, namely, (i) a nanodisk with two air channels and (ii) a nanodisk with three air channels. The air-channel positions are perturbed to observe and study the BICs in these designs. As illustrated in Figure 1b, both air channels are shifted in the negative ydirection from the center of the nanodisk. In contrast, in Figure 1c, the third air channel is introduced with a slightly different radius, $r_{\rm in}$ + $\Delta r_{\rm 1}$, forming equilateral vertices. The optimized parameters of the unit cell are $P_x = P_y = 820$ nm, r_{out} = 370 nm, r_{in} = 80 nm, g = 75 nm, and t = 350 nm, while the parameters s_v and Δr_1 are considered variable and discussed later. All numerical simulations are performed using COMSOL with periodic boundary conditions in the x and y directions and perfectly matched layers in the z-direction of the unit cell with dispersive silicon (Si).55 The refractive index of the substrate (Sapphire) is 1.74.

3. RESULTS AND DISCUSSION

3.1. Design 1: Nanodisk with Two Air Channels

The design of two air holes in the nanodisk without any shift in y (i.e., $s_y = 0$) exhibits $C_{2\nu}$ symmetry. It facilitates symmetry-protected BICs, as evident from eigenmode analysis (see Table S1 in the Supporting Information). The refractive index of silicon is fixed at 3.47, while the substrate is not considered in the eigenmode analysis.

When $s_y \neq 0$ nm, the $C_{2\nu}$ symmetry changes to C_s because all the rotational and mirror symmetries are broken, except for the mirror plane x = 0. The metasurface for the optimized parameters exhibits eight resonant modes, 1 to 8. Among these, resonant modes 1, 3, 5, 7, 6, and 8 are symmetry-protected

ACS Applied Optical Materials

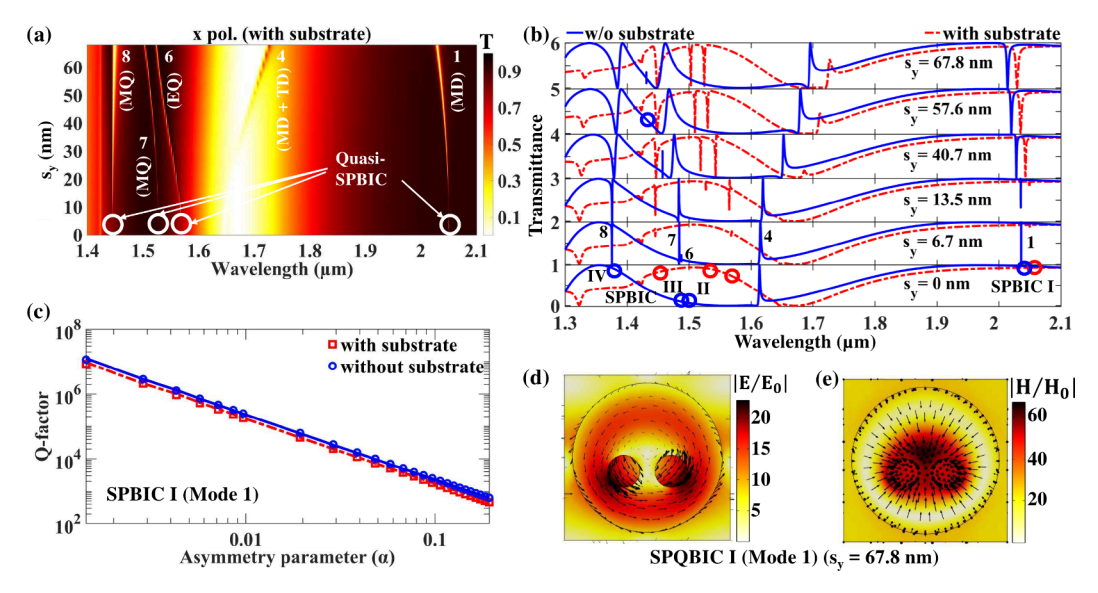


Figure 2. (a) Surface plot illustrating transmittance for various offset values of s_y when the incident light is x-polarized in the presence of a substrate. The quasi SPBICs are highlighted with open circles, and various modes along with the dominant multipole moments are also marked. (b) Transmittance line spectra for different asymmetry parameter values in both cases with and without substrate, highlighting the SPBICs (blue markers) and SPQBICs (red markers). (c) Q-factor of SPBIC (Mode 1), calculated using the Fano fitting formula. (d) Electric and (e) magnetic field intensity plots in a xy-plane along with the field vector distributions for SPQBIC (Mode 1) when $s_y = 67.8$ nm with the substrate.

BICs. Modes 1, 7, 6, and 8 are identified as SPBIC I, II, III, and IV for ease of reference and are marked in the plots. The dominant components of each resonant mode are determined through the Cartesian multipolar decomposition method (CMDM), ⁵⁶ viz. the magnetic dipole (MD) in Mode 1, magnetic quadrupole (MQ) in Modes 3, 7, and 8, and electric quadrupole (EQ) in Mode 6. The dominant multipoles in resonant modes 2, 4, and 5 are the toroidal electric moment (TED).

We introduced in-plane asymmetry to analyze the characteristics of BICs in the transmittance spectra. The QBICs are achieved by displacing the air channels from the center and shifting along the negative y-axis, as shown in Figure 2b. The shift of both air channels is achieved by varying the s_{ν} parameter (0 to 67.8 nm). Note that we consider a hypothetical scenario when there is no substrate. For the normal incidence of a plane wave with x polarization, the BIC transforms into QBICs, taking the form of a Fano resonances. As depicted in Figure 2a,b, as the shift s_v increases from 0 to 67.8 nm, the structure's symmetry is disrupted, causing the bound states to start interacting with the incoming radiation irrespective of a substrate. Thus, SPQBIC I, II, III, and IV start appearing in transmittance spectra both in the case without and with the substrate, as seen in Figure 2a,b. When the metasurface is placed on the substrate, the mirror symmetry in the z plane is broken, transforming the BICs to QBICs, along with the redshift of resonances; hence, there is no resonance crossing, as seen in Figure 2a where the SPQBICs are highlighted in white, whereas in the case without substrate, SPBIC II and SPBIC III experience resonance crossing at $s_y =$ 13.5 nm, leading to a swap of resonant modes with an exchange of their position in terms of wavelength. Following the resonance crossing, at around $s_v = 57.6$ nm, the SPBIC II demonstrates accidental BIC, vanishing of resonances in the transmittance spectra, as illustrated in Figure 2b.55

To quantitatively assess the level of asymmetry, we define the shift, s_v in terms of the dimensionless asymmetry parameter $\alpha = s_y/\sqrt{r_{\rm out}^2 - (r_{\rm in} + 0.5g)^2}$ where the parameter's values range from 0 to 1, representing the minimum and maximum shift scenarios. The Q-factor of the modes can be determined as ω_0/τ , where τ is the resonance line width obtained using the Fano formula mentioned in eq 1 and fitting the transmittance spectrum. The Fano fitting expression is given as described in ref 58

$$T_{\text{fano}}(\omega) = T_0(\omega) + A_0 \frac{(q + 2(\omega - \omega_0)/\tau)^2}{1 + (2(\omega - \omega_0)/\tau)^2}$$
 (1)

 T_0 is background scattering, ω_0 is resonance frequency, q is the Fano parameter, and A_0 is the coupling constant between the bright (continuum state) and dark (discrete state). As parameter α increases, the Q-factor of SPBIC I decreases, as shown in Figure 2c. The primary focus is on SPBIC I and how the introduction of air channels tailors its characteristics. Ideally, when $\alpha = 0$, BICs with an infinite Q-factor exist but cannot be observed in the transmittance spectra. The SPBIC I exhibits a maximum quality factor of 1.89×10^9 at $\alpha = 0$ for the freestanding structure. In numerical simulations with extremely high resolutions, the Q-factor can reach infinity, thus confirming the existence of a nonradiative BIC. At $\alpha = 0.193$ $(s_v = 67.8 \text{ nm})$, the SPBIC I yields a $Q \approx 650$ in the absence of the substrate, while in the presence of the substrate, it is 580. The interaction between SPBIC II and III is characterized by weak coupling. Specifically, the Q-factor of SPBIC II increases compared to SPBIC III, which experiences a decrease in the Qfactor as the crossing occurs with an increase in displacement of air channels from the center, governed by s_v (see Supplementary Figure S2). Upon examining symmetryprotected QBICs, the radiative Q-factor demonstrates an inverse quadratic relationship with the asymmetry parameter, α , represented as $Q_{\text{rad}} = k\alpha^{-2}$, where k denotes a proportionality constant. In Figure 2c, the fitted Q-factor of SPBIC I is depicted by square markers, illustrating its adherence to the relationship mentioned above in the presence and absence of a substrate.

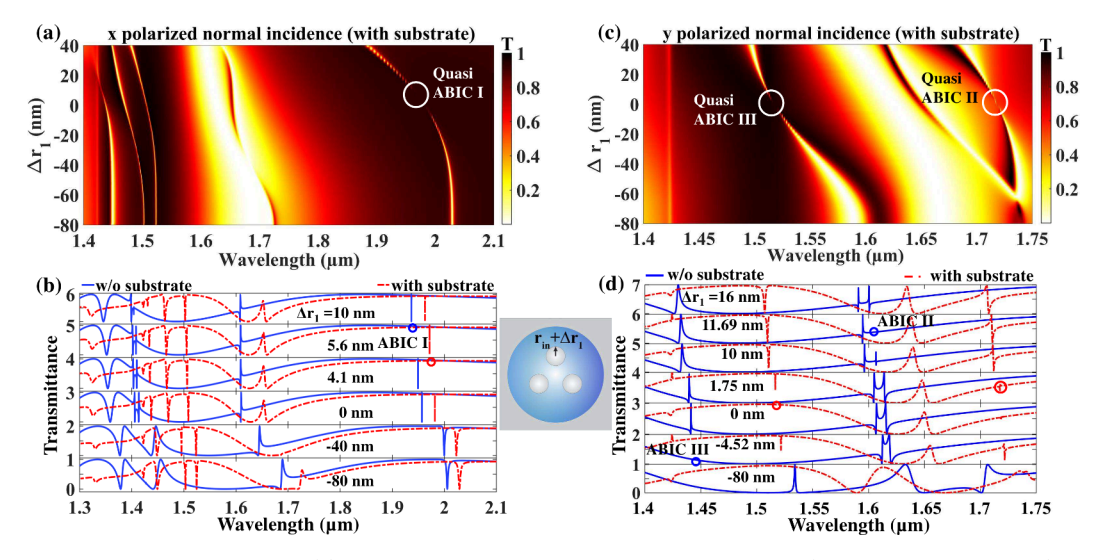


Figure 3. Transmittance under *x*-polarization: (a) surface plot illustrating the formation of AQBIC I (marked by an open circle) in the presence of substrate and (b) line plot of transmittance with and without substrate. Transmittance under *y*-polarization (c) surface plot indicating AQBIC II and AQBIC III (marked by open circles) in the presence of substrate, and (d) line plot demonstrating the comparison with and without substrate case. The blue and red circles show the formation of ideal ABIC and AQBIC in the case with and without substrate, respectively. The inset shows the unit cell of a nanodisk resonator with three air channels.

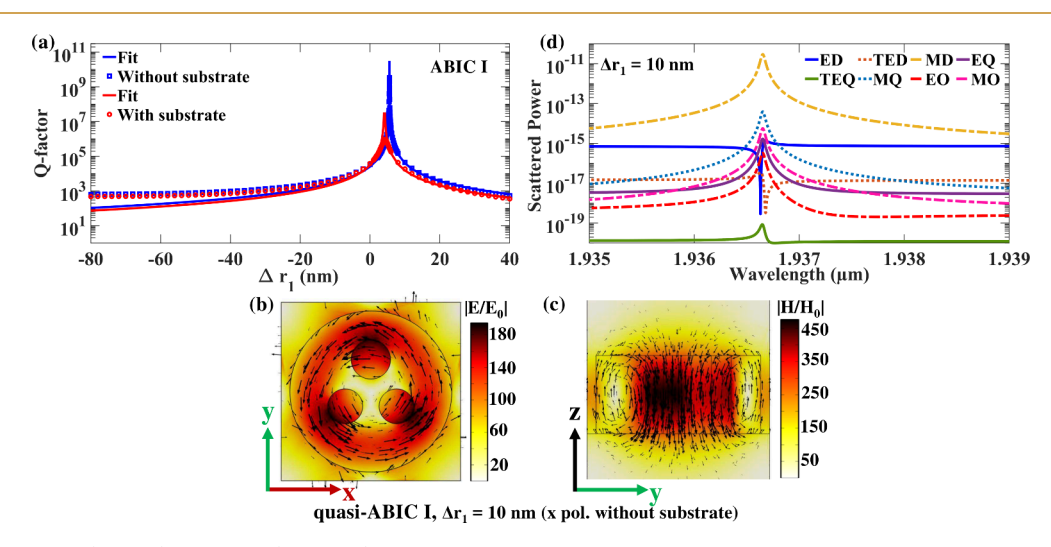


Figure 4. (a) Simulated (marker) and fitted (solid line) *Q*-factor for ABIC I with and without substrate. The normalized electric field distribution in the *xy*-plane is shown in (b), while (c) illustrates the normalized magnetic field distribution in the *yz*-plane. (d) Multipolar distribution plot of AQBIC I when $\Delta r_1 = 10$ nm, without substrate. In this context, TEQ, EO, and MO represent toroidal electric quadrupole, electric octupole, and magnetic octupole, respectively.

While investigating the quasi-BIC nature of the modes, we can utilize multipolar decomposition to calculate the scattered power through the displacement current density in the nanodisk resonator. For SPBIC I, in the absence of a substrate, when air channels are displaced by $s_y = 67.8$ nm, the quasi-BIC emerges at $\lambda = 2.013 \ \mu m$. The CMDM analysis reveals that, at quasi-BIC, the z-component of the magnetic dipole moment is dominant, while the other moments are negligible (see Supplementary Figure S3), which holds even in the presence of a substrate. Additionally, the near-field distribution in the x-y plane suggests circular electric field lines and out-of-plane magnetic lines, which lead to the dominant z-component of the magnetic field, as shown in Figure 2d,e. It is evident from Figure 2e that there is a significant magnetic field enhancement $(|H/H_0| \approx 67)$ when the substrate is present in the case of SPBIC I. The magnetic field enhancement increases in the absence of the substrate (see Supplementary Figure S4a,b).

The magnetic field becomes highly confined with a decrease in the asymmetry parameter. As an example, for asymmetry, $\alpha = 1\%$, the quasi-BIC induces a field enhancement 1000 times (see Supplementary Figure S4c,d). Note that in the case of a *y*-polarized incidence, the metasurface supports resonant modes 3, 4, and 5. Among these, modes 3 and 5 are SPBICs that appear in the transmittance spectra when the air channels are displaced from the center (Supplementary Figure S5).

3.2. Design 2: Three Air Channels Nanodisk Resonator

As mentioned earlier, one has to have accurate control of the asymmetry parameters to achieve SPBIC with a high Q, which poses a fabrication challenge. To alleviate this constraint, we study the development of accidental BICs, which demonstrate a very high Q-factor and can be achieved with simple design parameters. As observed in the previous section, the Q-factor of SPQBIC decreases quadratically with the increase in the

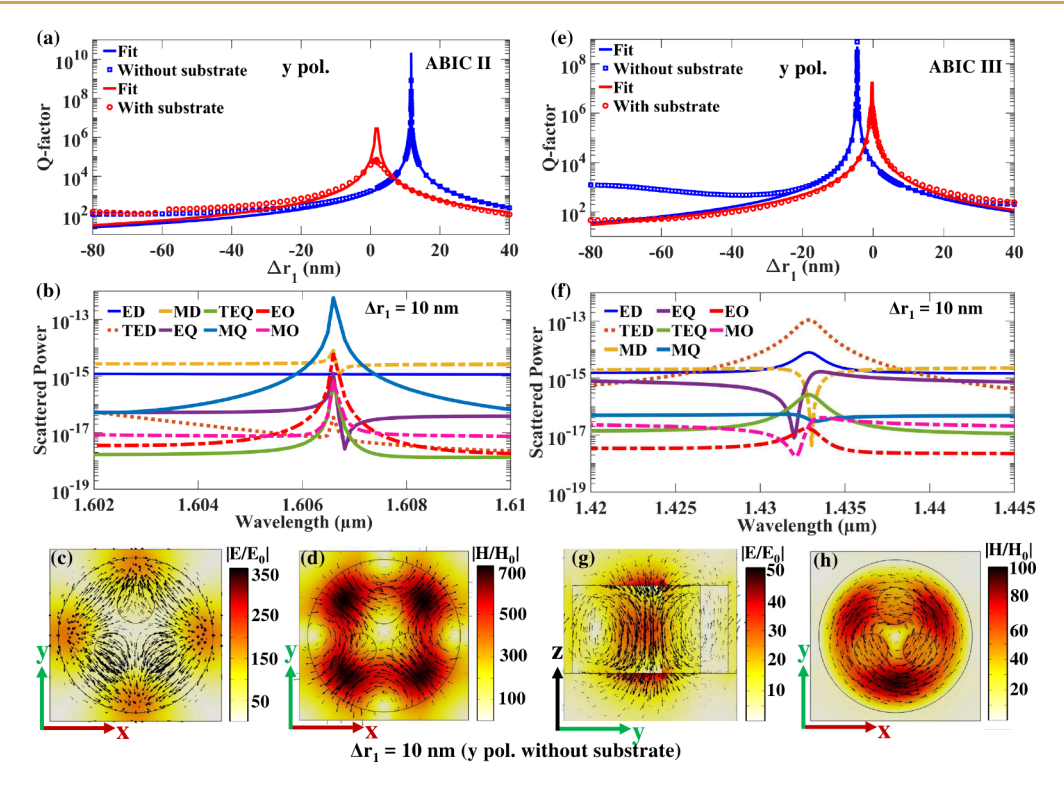


Figure 5. Panels (a) and (e) depict the simulated Q-factor (marker) and the fitted Q-factor (solid curve) for both ABIC II and ABIC III with and without substrate. The multipolar content when $\Delta r_1 = 10$ nm without substrate for (b) AQBIC II and (f) AQBIC III. Normalized electric field distribution (intensity and arrow plot) is shown in (c) the xy-plane for AQBIC II and (g) the yz-plane for AQBIC III without substrate. Normalized magnetic field intensity and arrow plot distribution in the (d) xy-plane for AQBIC III and (h) xy-plane for AQBIC III without substrate.

asymmetry parameter. Therefore, we modify the nanodisk resonator design by introducing the third air channel into the nanodisk to transform the SPQBIC to AQBIC, where the Qfactor remains high even for a greater degree of structural perturbation. To observe the formation of ABICs, we modified the structure of two air channels in the disk and introduced a third air channel, as depicted in Figure 1c. This design is similar to our earlier work in ref 59, where the structure had different dimensions and was placed on a silica substrate. In this study, we used sapphire as the substrate. The placement of the third air channel inside the disk was such that an imaginary line connecting the center of all air channels formed an equilateral triangle, with its center coinciding with the center of the Si nanodisk. The radius of the third disk was taken as $r_{\rm in}$ + Δr_1 , and the gap (g) between all the air channels is equal, while all other parameters remained the same as above. By increasing or decreasing Δr_1 , we can control the radius of the third air channel. To achieve optimal accidental BICs, it is crucial to maintain reflection symmetry in the z = 0 plane, as emphasized in ref 60. Therefore, the metasurface is considered freestanding in a uniform air environment and illuminated normally with xand y-polarized light.

3.2.1. *x*-Polarized Incidence. In this subsection, we analyze the metasurface constituted by the nanodisk resonators with triple air channels when the *x*-polarized plane wave is incident normally. When the radius of the third air channel is changed by Δr_1 , the triple air channel nanodisk resembles a two air-channel nanodisk at $\Delta r_1 = -80$ nm, corresponding to the situation as $s_y = 67.8$ nm, where all the resonant modes remain the same as that of two air-channels. As Δr_1 increases, the transmittance spectra in Figure 3b show that the line width of resonant mode 1 near $\lambda = 2 \mu m$ gradually decreases and

disappears at $\Delta r_1 = 5.6$ nm (indicated by the open circle) in the case of no substrate. The resonant mode 1 reappears later with a gradually increasing line width, suggesting the emergence of ABIC I. This assertion can be further supported by examining the Q-factor for ABIC I, obtained through eigenmode analysis and depicted as a function of Δr_1 in Figure 4a. It is clear that as Δr_1 approaches 5.6 nm, the Q-factor tends toward infinity and demonstrates an inverse quadratic relationship with Δr_1 . Simulation results are fitted with Q $\propto 1/(\Delta r - \Delta r_{\rm BIC})^2$, confirming the presence of the ideal ABIC in theory. The presence of the ABIC within the specified framework can be comprehended physically by analyzing the near-field distribution of the electromagnetic field and CMDM.⁵⁶ The ABIC I transforms into quasi-ABIC I (AQBIC I) at $\Delta r_1 = 10$ nm. From Figure 4b,c, it is evident that the electric field rotates within the xy plane of the nanodisk resonator, resulting in the generation of an out-ofplane magnetic dipole (MD) in the yz plane, while the circulating magnetic field in the yz plane signifies the development of an in-plane electric dipole (ED). This observation can be corroborated through a CMDM analysis. Figure 4d demonstrates that the dominant multipoles consist of out-of-plane MD as well as other out-of-plane magnetic multipoles like MQ and magnetic octupole (MO), along with comparatively weaker in-plane electric multipoles such as EQ, electric octupole (EO), ED, TED, and toroidal electric quadrupole (TEQ). These in-plane electric multipoles and out-of-plane magnetic multipoles combine to generate a TEpolarized wave at a specific geometrical parameter and destructively interfere with each other in the parameter space, as is the case with $\Delta r_1 = 5.6$ nm, resulting in the formation of the nonradiating ideal infinite Q-factor ABIC.⁶¹

We further examine the impact of incorporating the sapphire substrate beneath the metasurface. The substrate introduces an extra leakage channel by breaking the vertical symmetry, 62 leading to the emergence of both odd and even multipoles for a specific resonant mode. Additionally, all resonant modes experience a red shift compared with the scenario without the substrate. As Δr_1 increases in the metasurface with the substrate, the resonant mode 4 around $\lambda = 1.68 \ \mu m$ weakly interacts with the bright background mode and diminishes around $\Delta r_1 = -38$ nm, as illustrated in Figure 3a. The increase in Δr_1 results in the strong coupling of a broad bright mode in the background with the dark Fano resonant mode 4, leading to the formation of EIT, 63,64 as depicted in Figure 3a,b. At Δr_1 = 10 nm, EIT at λ = 1.651 μ m exhibits a Q-factor of 245. For the resonant mode 1, the resonance becomes narrower as Δr_1 increases, and the mode disappears around $\Delta r_1 = 4.1$ nm (represented by an open circle in Figure 3a,b), indicating the presence of AQBICs. It re-emerges with enhanced line width. In the presence of a substrate, the Q-factor has a finite value of 10^5 around $\Delta r_1 = 4.1$ nm and displays an inverse quadratic relation with varying Δr_1 . The breaking of vertical symmetry transforms the ideal ABIC into a supercavity mode, resulting in a finite Q-factor value near the vanishing point.

Note that when $\Delta r_1=10$ nm, resonant mode 1 demonstrates a Q-factor of approximately 44,000 at a wavelength of $\lambda=1.936~\mu{\rm m}$ in the absence of the substrate. Even in the presence of the substrate, the Q-factor decreases by a factor of 2.5, possessing a high magnetic field enhancement of $|H/H_0| \approx 305$ (see Supplementary Figure S6c,d). For $\Delta r_1=0$ nm, the metasurface with substrate shows a high Q-factor of approximately 38000, resulting in a high magnetic field enhancement ($|H/H_0| \approx 504$, see Supplementary Figure S6 a,b). Furthermore, the nanodisk with a third air channel of radius = 80 nm ($\Delta r_1=0$ nm) and 90 nm ($\Delta r_1=10$ nm) is easy to fabricate.

3.2.2. y-Polarized Incidence. Similarly, when a plane wave of light polarized in the y-direction interacts with a metasurface composed of nanodisk resonators with three air channels where $\Delta r_1 = -80$ nm (resembling two air channels with $s_v = 67.8$ nm with same mode numbers for y-polarized incidence), the standalone metasurface (i.e., without substrate) displays an EIT mode at $\lambda = 1.535 \mu m$ and two Fano resonances at $\lambda = 1.633 \ \mu m$ and $\lambda = 1.706 \ \mu m$ with opposite polarities. As the Δr_1 increases, the Fano resonance close to 1.7 µm shifts toward the blue end of the spectrum and weakly interacts with the Fano resonance near 1.6 μ m. This weak interaction causes the resonances to intersect at $\Delta r_1 = -14$ nm. Consequently, at $\Delta r_1 = -12$ nm, the destructive interference between the resonances gives rise to a new phenomenon known as EIT at $\lambda = 1.623 \ \mu m$. As Δr_1 continues to increase, the resonances decouple, leading to the narrowing and eventual disappearance of the resonance at $\lambda = 1.606 \ \mu m$ and at $\Delta r_1 = 11.69$ nm. This disappearance results in the formation of an ideal ABIC II (indicated by an open blue circle), as shown in Figure 3d. Similarly, at $\Delta r_1 = -4.52$ nm, the EIT resonances around $\lambda = 1.53 \mu m$ vanish, creating an ideal ABIC III. Upon further increasing the Δr_1 value, we observe the reappearance of quasi-ABIC II (AQBIC II) and quasi-ABIC III (AQBIC III) resonances. Figure 5a,b reveals that the Q-factor tends to approach infinity at $\Delta r_1 = 11.69$ nm and $\Delta r_1 = -4.52$ nm for both ABIC II and ABIC III, respectively. Additionally, the Q-factor demonstrates an inverse quadratic relationship with Δr_1 , indicating the presence of ideal ABIC. The origins of ABIC II and ABIC III can be comprehended through multipolar decomposition and near-field intensity distribution.

For $\Delta r_1 = 10$ nm, AQBIC II demonstrates a quadrupolar nature in the xy-plane as shown in Figure 5c,d, with a magnetic quadrupole to be the dominant multipole (Figure 5b). At the same time, AQBIC III arises due to the resonance's toroidal nature. The analysis of Figure 5g reveals that in the yz-plane, the electric dipole aligns along the z-axis, while the magnetic field circulates in the xy-plane, resulting in the generation of a magnetic dipole along the x-axis (Figure 5h). Consequently, the toroidal moment is produced along the z-axis. That is further supported by Figure 5f, where the dominant multipole is identified as TED. Thus, ABIC III can be identified as accidental BIC resulting from the destructive interference of TED, ED, MQ, and other weak multipoles such as EQ and MD.

We learned from the x-polarized incidence that introducing a substrate beneath the metasurfaces causes the resonances to red-shift and disrupts the vertical symmetry of the structure, resulting in the transformation of the ideal ABIC to AQBIC. Consequently, in the presence of the substrate, when $\Delta r_1 = -80$ nm, EIT is observed at $\lambda = 1.613$ μ m, while the other two resonances are weakly linked around $\lambda = 1.735$ μ m. Moreover, resonance crossing occurs at $\Delta r_1 = -68$ nm, leading to the emergence of EIT at $\Delta r_1 = -60$ nm and at $\lambda = 1.735$ μ m. The intensity of EIT increases, and it acquires the Fano line shape, as depicted in Figure 3c,d. With a further increase in the parameter Δr_1 , the Fano resonance at approximately 1.72 μ m and resonance at 1.54 μ m display AQBIC behavior at $\Delta r_1 = 1.75$ nm and $\Delta r_1 = 0$ nm (indicated by white and red open circles in Figure 3c,d).

In a practical scenario involving a substrate, both AQBIC II and AQBIC III exhibit a finite Q-factor at $\Delta r_1 = 1.75$ nm and $\Delta r_1 = 0$ nm, respectively. At $\Delta r_1 = 0$ nm, the resonances have a Q-factor of 37845 for AQBIC II and 8.90×10^5 for AQBIC III, accompanied by the magnetic field enhancement, $|H/H_0|$ lof 280 and 2098, and electric field enhancement, $|E/E_0|$ of 162 and 1530, respectively (see Supplementary Figure S7a,b and Figure S8a,b). Meanwhile, at $\Delta r_1 = 10$ nm, the resonances exhibit Q-factors of 2950 for AQBIC II and 2170 for AQBIC III, with magnetic field enhancements, $|H/H_0|$ of 135 and 131, and electric field enhancements, $|E/E_0|$ of 78 and 93, respectively (see Supplementary Figure S7c,d and Figure S8c,d).

4. CHIRALITY IN HOLLOW AIR CHANNELS NANODISK RESONATOR

In this section, we study the chiroptical response of the hollowair channel-aided metasurface, both extrinsic and intrinsic chirality. In order to understand the chiral response, we analyze $e^{-i\omega t}$, a time-dependent wave propagating in the negative z direction, which represents circularly polarized light as $1/\sqrt{2}\left(E_x\pm iE_y\right)$. Here, + denotes right circularly polarized light (RCP), while – indicates left circularly polarized light (LCP). The chirality is determined by circular dichroism, which is defined as the difference between the transmittance of RCP and LCP incidences: 49

$$CD = \frac{(T_{rr} + T_{lr}) - (T_{ll} + T_{rl})}{(T_{rr} + T_{lr}) + (T_{ll} + T_{rl})}$$
(2)

where r represents RCP and l represents LCP, respectively.

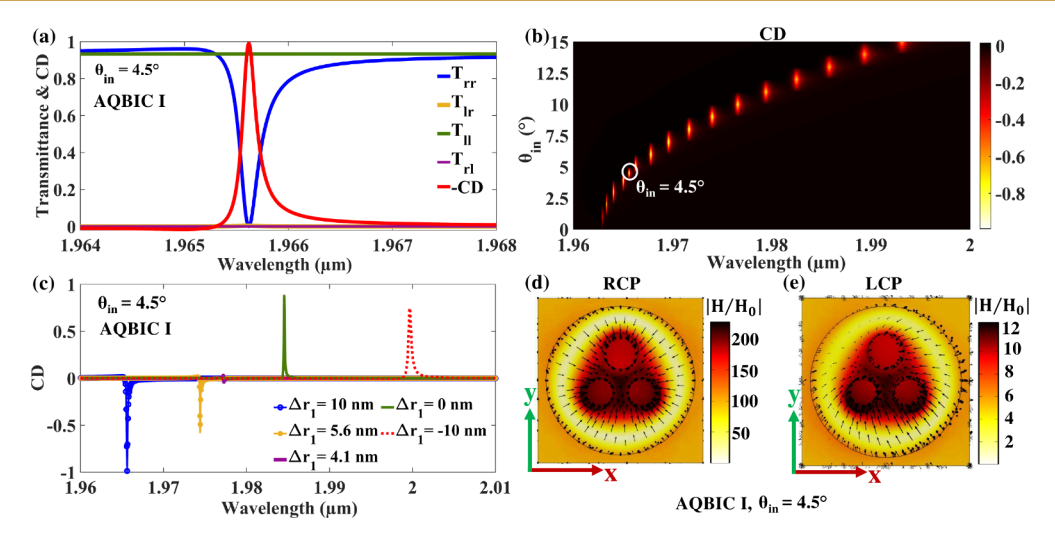


Figure 6. Extrinsic chiroptical characteristics of AQBIC I of nanodisk with three air channels under oblique incidence. (a) Transmittance plot (T_{rr}, T_{lb}, T_{rl}) and - CD when $\Delta r_1 = 10$ nm and $\theta_{in} = 4.5^{\circ}$, (b) variation of CD for transmitted waves under various incident angles at a fixed $\Delta r_1 = 10$ nm. (c) The CD at a fixed angle of incidence $\theta_{in} = 4.5^{\circ}$, while the Δr_1 varies. The near magnetic field distribution of the chiral AQBIC resonance in the xy plane for (d) RCP and (e) LCP incidence.

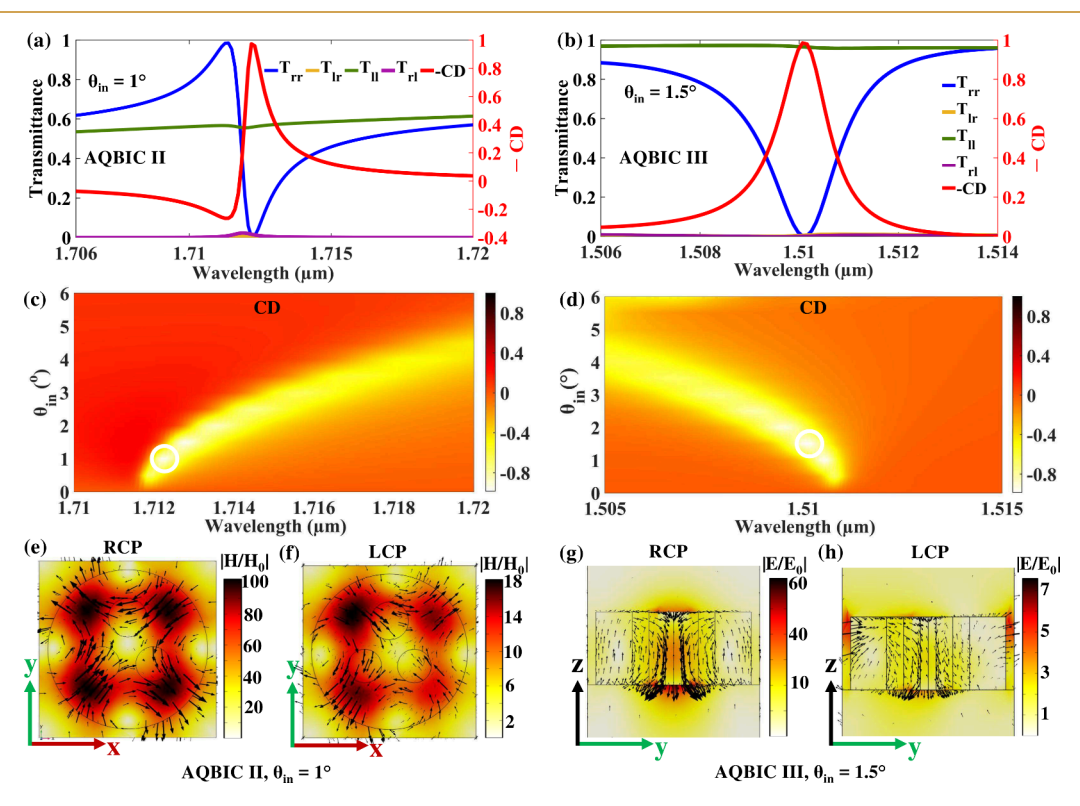


Figure 7. Extrinsic chiroptical characteristics of AQBIC II and III of nanodisks with three air channels at oblique incidence. Transmittance plot $(T_{rr}, T_{lr}, T_{lr}, T_{lr}, T_{lr}, T_{lr}, T_{lr}, T_{lr}, T_{lr})$ and - CD when $\Delta r_1 = 10$ nm and (a) $\theta_{in} = 1^{\circ}$ for AQBIC II and (b) $\theta_{in} = 1.5^{\circ}$ for AQBIC III. Variation of CD for transmitted waves at $\Delta r_1 = 10$ nm for varying angle of incidence for (c) AQBIC II and (d) AQBIC III. The near magnetic field distribution of the chiral AQBIC II resonance in the xy plane for (e) RCP and (f) LCP incident light. The near electric field distribution of the chiral AQBIC III resonance in yz-plane for (g) RCP and (h) LCP incident light.

First, we analyze extrinsic chirality in a nanodisk with two air channels for SPBIC I (see Supplementary Figure S9) where it is found that for an incidence angle of $\theta_{\rm in}=22^{\circ}$, a dip appears in transmittance spectrum for LCP light, $T_{ll}=0.045$ at 2.086 μ m. Also, the transmittance of RCP is $T_{rr}=0.55$ along with nearly equal cross-polarized components, $T_{lr}=0.17$ and $T_{rl}=0.15$ that results in maximum chirality, CD = 0.57 and Q-factor = 641. It can be inferred that incoming LCP light strongly

couples with the nanostructure, but the same is true for the RCP along with their cross-polarization component, which reduces the overall chirality of the system. This is also supported by the electric and magnetic field plots at resonance wavelength, where the field enhancement in both RCP and LCP is weak and is on the order of 1. However, it is possible to enhance the extrinsic chirality by introducing the third air channel in the nanodisk.

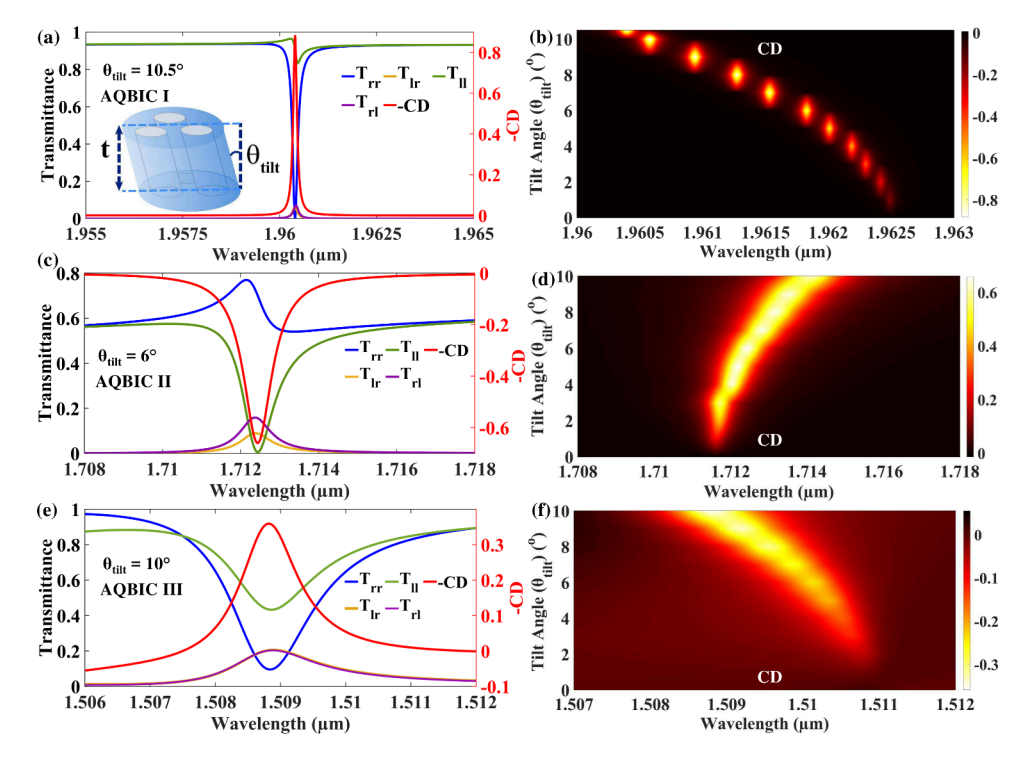


Figure 8. Intrinsic chiroptical characteristics of AQBIC I, II and III of tilted nanodisk with three air channels at normal incidence. Transmittance plot $(T_{rr}, T_{lr}, T_{ll}, T_{rl})$ and - CD when $\Delta r_1 = 10$ nm and (a) $\theta_{tilt} = 10.5^{\circ}$ for AQBIC I. Inset shows the schematic of geometrical manipulation of the hollowed nanodisk to realize intrinsic chirality, (c) $\theta_{tilt} = 6^{\circ}$ for AQBIC II and (e) $\theta_{in} = 10^{\circ}$ for AQBIC III. Variation of CD for transmitted waves at $\Delta r_1 = 10$ nm for varying tilt angle (θ_{tilt}) (b) AQBIC I, (d) AQBIC II, and (f) AQBIC III.

As discussed earlier, the nanodisk with three air channels demonstrates mirror symmetry along the yz plane. This symmetry persists even when the radius (Δr_1) varies. Consequently, the structure displays achiral behavior under the normal incidence of circularly polarized light. To demonstrate chiral response, all mirror symmetries present in the structure are broken by changing the angle of incidence, i.e., oblique incident. The angle of incidence, $\theta_{\rm in}$, lies in the xz-plane between the incident light and the z-axis, resulting in the breaking of mirror symmetry in the yz-plane as well as the out-of-plane mirror symmetry. Therefore, combining an achiral metasurface with an oblique incidence creates a chiral AQBIC metasurface.

In the case of AQBIC I, when circularly polarized light is incident at an angle of $\theta_{\rm in} = 4.5^{\circ}$ and $\Delta r_1 = 10$ nm, it can be observed from Figure 6a that a resonant dip occurs at 1.9656 μ m for the RCP copolarized transmittance, T_{rr} . At the same time, the LCP copolarized transmittance, T_{lb} remains close to 0.92. Additionally, the cross-polarized transmittance components, T_{lr} and T_{rb} are negligible and less than 0.05 within the resonance range, resulting in a giant CD of -0.99 and a Q-factor of 8846. In Figure 6b, it is evident that as $\Delta r_1 = 10$ nm, the circular dichroism increases and reaches its maximum at a $\theta_{\rm in}$ of 4.5° , after which it decreases with the increase in incident angle. It indicates that incident angle less than and greater than 4.5° result in weaker chirality. The structure transmits the LCP light while the RCP light is reflected.

The magnetic field intensity plot depicted in Figure 6d illustrates a considerable enhancement of magnetic field confinement by a factor exceeding 200 under RCP illumination. In contrast, it is notably weaker under LCP illumination (Figure 6e). Here, the out-of-plane magnetic field distribution from Figure 6d confirms the dominance of the

MD moment, which is consistent with the observation made from the multipole decomposition of AQBIC I for x-polarized illumination. The planar design employed here facilitates maximum chirality, even with varying Δr_1 , as evident from Figure 6c. When circularly polarized light is incident at $\theta_{\rm in}$ = 4.5° and Δr_1 is varied, a negative value of circular dichroism is observed for positive Δr_1 , indicating coupling between RCP and AQBIC, while LCP remains isolated. Conversely, a decrease in Δr_1 results in a positive value of CD, indicating coupling between LCP and AQBIC, while the RCP is suppressed.

It is noticed that both the AQBIC II and AQBIC III resonances can also exhibit giant extrinsic chirality at $\Delta r_1 = 10$ nm, similar to the extrinsic chirality in AQBIC I. Figure 7a,b illustrates the extrinsic chirality induced in the metasurface when circularly polarized light is incident at an oblique angle. In the case of AQBIC II (Figure 7a), the metasurface exhibits a giant chirality of -0.97 at $\theta_{in} = 1^{\circ}$, whereas AQBIC III reveals a high chiral response of -0.98 for $\theta_{in} = 1.5^{\circ}$. The AQBIC II and III yield Q-factors of 2114 and 894, respectively. As the angle of incidence varies while Δr_1 fixed at 10 nm, in both the cases of AQBIC II and AQBIC III, we observe that CD has its maxima at 1° and 1.5° and decreases before and after this incident angles (Figure 7c,d). This implies weaker coupling of LCP with the AQBICs. The chiral AQBIC II and AQBIC III resonant modes exhibit MQ and TED nature, as observed from near magnetic and electric field intensity and arrow plot shown in Figure 7e—h. Since RCP is strongly coupled to the resonant modes, we can observe high magnetic and electric field enhancements of 100 and 60 for chiral AQBIC II and AQBIC III from Figure 7e,g, whereas in the case of the LCP, the resonant modes have reduced magnetic and electric field enhancement that can be observed from Figure 7f,h.

It is important to know that an ultrahigh Q-factor chiral response can be achieved for AQBIC I, II, and III for certain values of Δr_1 and $\theta_{\rm in}$, but at the expense of nonunity CD. To illustrate this, Δr_1 and $\theta_{\rm in}$ are varied for AQBIC I mode, where the Q-factor is ≈ 19519 , but the CD value is reduced to ≈ 0.94 when $\Delta r_1 = 0$ nm and $\theta_{\rm in} = 3.1^\circ$. Similarly, for $\Delta r_1 = 5.6$ nm and $\theta_{\rm in} = 1.35^\circ$, an ultrahigh Q-factor $\approx 10^5$ is observed; however, CD degrades and come to ≈ -0.86 (see Supplementary Figure S10).

This study is not only limited to the observation of extrinsic chiral response by varying the angle of incidence but also studies the intrinsic response of the nanostructure by manipulating the structural design in such a manner that the symmetries that were present earlier in the case of extrinsic chirality vanish. One of the possible approaches to attain intrinsic chirality in the proposed metasurface is to introduce a tilt ($\theta_{\rm tilt}$) in the nanodisk resonator, as shown in the inset of Figure 8a. All of the geometrical parameters remain the same, with $\Delta r_1 = 10$ nm. Note that, earlier, the center of the nanodisk with three air channels was concentric to the square lattice, which is now shifted in the *x*-axis by 33 nm to accommodate the tilt angle until $\theta_{\rm tilt} = 10.5^{\circ}$.

The introduction of the tilt in the geometry breaks the outof-plane and in-plane symmetry; in this case, symmetry in the yz-plane makes the structure intrinsically chiral. It is observed from Figure 8a that for $\theta_{\rm tilt}$ = 10.5° and normal incidence, the metasurface composed of tilted nanodisks strongly couples with the RCP, yielding a dip in transmittance spectra, whereas it weakly couples with the LCP such that the LCP is transmitted through the nanostructure. The CD is negligible when $\theta_{\text{tilt}} = 0^{\circ}$. As the θ_{tilt} increases as seen from Figure 8b, the CD also increases, signifying the coupling of the metasurface with one polarization component. A maximum CD (= -0.88)and Q-factor \approx 12300 has been achieved for $\theta_{\text{tilt}} = 10.5^{\circ}$. Similarly, in the case of AQBIC II, when the nanodisk tilt increases until $\theta_{\text{tilt}} = 6^{\circ}$, CD increases, after which CD starts decreasing as seen from Figure 8d. However, we observe that the metasurface strongly interacts with the LCP and weakly with the RCP, while cross-polarized components are present (see Figure 8c), which is different from the intrinsic chiral response of AQBIC I and AQBIC III. The AQBIC II exhibits a CD = 0.65 with a Q-factor = 1691 for $\theta_{\text{tilt}} = 6^{\circ}$. In the case of AQBIC III, the intrinsic chiral response is not very strong, as observed from Figure 8e,f. The CD reaches a maximum value of -0.35 and Q-factor of 985 as the $\theta_{\rm tilt}$ increases. Figure S11 in Supporting Information depicts the near-field distribution in the designed tilted metasurface exhibiting intrinsic chirality for AQBIC I-III.

Based on the analysis, it can be inferred that the nanodisk with the three air channels transmits the LCP light, while the RCP light is reflected. This suggests that precise incident angle adjustment facilitates efficient coupling of AQBICs with the RCP but not with the LCP in the case of extrinsic chirality with a near-unity CD of high Q-factor. In the case of intrinsic chirality for a specific tilt angle, AQBIC I and AQBIC III exhibit chirality such that LCP is transmitted and RCP is reflected, but in the case of AQBIC II, RCP is transmitted, while LCP is reflected. Therefore, these findings emphasize the maximum chiroptical response to the changes in the incident angle and geometric asymmetries and modifications.

In Table S2 (see Supporting Information), we have summarized recent work on the chiral quasi-BIC metasurfaces on the basis of the type of BICs, number of resonant modes, Q- factors, and CDs and compared it to the work presented in this paper. Clearly, most of the work is done in intrinsic chirality with a high *Q*-factor and CD utilizing the concept of SPBICs. In comparison to the existing works, our work highlights multiple AQBIC with a high intrinsic and extrinsic chiroptical response (near unity CD and high *Q*-factor).

5. CONCLUSIONS

To summarize, we have demonstrated the incorporation of air channels within nanodisk resonator-based dielectric metasurfaces to enable multiple symmetry-protected and accidental BICs, depending on the design configuration. Specifically, a design with three air channels enables accidental BICs for both x- and y-polarized light by tuning the radius of the third air channel. Additionally, we explored the numerical behavior of achiral metasurfaces with yz-plane symmetry, capable of supporting AQBICs and displaying a strong extrinsic chiroptical response by breaking mirror symmetry under oblique incidence. The strong intrinsic chirality is also exhibited by tilting the nanodisk. By integrating multiple air channels into Si nanodisks, we achieved enhanced multispectral chirality, resonance tunability, a high Q-factor, and significant field enhancement with minor parameter adjustments, while maintaining fabrication simplicity. The potential applications of these chiral metasurfaces include chiral sensing, chiral spectroscopy, spin-selective imaging and optical devices, and nonlinear optics. Beyond BICs, the metasurfaces also support EIT resonances, offering promising avenues for slowlight applications.

ASSOCIATED CONTENT

Supporting Information

The Supporting Information is available free of charge at https://pubs.acs.org/doi/10.1021/acsaom.4c00489.

Section S1: eigenmode analysis of and radiation pattern of two air-channels nanodisk resonator; Section S2: Quality factor of 3 SPBIC for x-polarization incidence; Section S3: Multipole decomposition of all the modes for x-polarization incidence in nanodisk with two air channels; Section S4: Electric and magnetic field plot in nanodisk with two air channels; Section S5: Transmittance and quality factor plots for two air-channel nanodisk resonator metasurface for y-polarization incidence; Section S6: Electric and magnetic field plot in nanodisk with three air channels for ABIC I, ABIC II, and ABIC III in case of substrate; Section S7: Extrinsic chirality in SPBIC I in nanodisk with two air channels; Section S8: Extrinsic chirality in ABIC I in nanodisk with three air channels for varying Δr_1 ; Section S9: Field plots in tilted nanodisk with three air channels for intrinsic chirality when $\Delta r_1 = 10$ nm for AQBIC I, II, and III; Section S10: Comparative table depicting the advantages of the current work (PDF)

■ AUTHOR INFORMATION Corresponding Author

Shubhanshi Sharma — Department of Electronics and Electrical Communication Engineering, Indian Institute of Technology Kharagpur, Kharagpur, West Bengal, India 721302; orcid.org/0000-0002-7618-2774; Email: shubhanshi07@iitkgp.ac.in

Authors

Alina Karabchevsky — School of Electrical and Computer Engineering, Ben-Gurion University of the Negev, Beer-Sheva 8410501, Israel; Department of Physics, Lancaster University, Lancaster LA1 4YB, United Kingdom; orcid.org/0000-0002-4338-349X

Shailendra K. Varshney – Department of Electronics and Electrical Communication Engineering, Indian Institute of Technology Kharagpur, Kharagpur, West Bengal, India 721302

Complete contact information is available at: https://pubs.acs.org/10.1021/acsaom.4c00489

Notes

The authors declare no competing financial interest.

ACKNOWLEDGMENTS

The authors acknowledge the technical discussions with Monica Pradhan, School of Nanoscience and Technology, Indian Institute of Technology, Kharagpur. This research was supported by the DST Govt. of India, vide no: DST/INT/ISR/P-34/2023 and SPARC/2024-2025/NXTG/P3840 by the Ministry of Education Govt. of India.

REFERENCES

- (1) Kamali, S. M.; Arbabi, E.; Arbabi, A.; Faraon, A. A review of dielectric optical metasurfaces for wavefront control. *Nanophotonics* **2018**, *7*, 1041–1068.
- (2) Sharma, S.; Pradhan, M.; Yadav, A.; Varshney, S. K. Visible to Infrared Dielectric Metasurfaces and their Applications. *Indian Journal of Pure & Applied Physics (IJPAP)* **2023**, *61*, 568–588.
- (3) Kuznetsov, A. I.; et al. Roadmap for Optical Metasurfaces. ACS Photonics 2024, 11, 816–865.
- (4) Chen, H.-T.; Taylor, A. J.; Yu, N. A review of metasurfaces: physics and applications. *Rep. Prog. Phys.* **2016**, *79*, 076401.
- (5) Azzam, S. I.; Kildishev, A. V. Photonic Bound States in the Continuum: From Basics to Applications. *Advanced Optical Materials* **2021**, *9*, 2001469.
- (6) Hsu, C. W.; Zhen, B.; Stone, A. D.; Joannopoulos, J. D.; Soljačić, M. Bound states in the continuum. *Nature Reviews Materials* **2016**, *1*, 1–13.
- (7) Zhou, C.; Huang, L.; Jin, R.; Xu, L.; Li, G.; Rahmani, M.; Chen, X.; Lu, W.; Miroshnichenko, A. E. Bound States in the Continuum in Asymmetric Dielectric Metasurfaces. *Laser Photonics Reviews* **2023**, *17*, 2200564.
- (8) Zhou, Q.; Fu, Y.; Huang, L.; Wu, Q.; Miroshnichenko, A.; Gao, L.; Xu, Y. Geometry symmetry-free and higher-order optical bound states in the continuum. *Nat. Commun.* **2021**, *12*, 4390.
- (9) van Hoof, N. J.; Abujetas, D. R.; ter Huurne, S. E.; Verdelli, F.; Timmermans, G. C.; Sánchez-Gil, J. A.; Rivas, J. G. Unveiling the Symmetry Protection of Bound States in the Continuum with Terahertz Near-Field Imaging. *ACS Photonics* **2021**, *8*, 3010–3016.
- (10) Li, Z.; Zhou, L.; Liu, Z.; Panmai, M.; Li, S.; Liu, J.; Lan, S. Modifying the Quality Factors of the Bound States in the Continuum in a Dielectric Metasurface by Mode Coupling. *ACS Photonics* **2023**, *10*, 206–216.
- (11) Abujetas, D. R.; Olmos-Trigo, J.; Sánchez-Gil, J. A. Tailoring Accidental Double Bound States in the Continuum in All-Dielectric Metasurfaces. *Advanced Optical Materials* **2022**, *10*, 2200301.
- (12) Bogdanov, A. A.; Koshelev, K. L.; Kapitanova, P. V.; Rybin, M. V.; Gladyshev, S. A.; Sadrieva, Z. F.; Samusev, K. B.; Kivshar, Y. S.; Limonov, M. F. Bound states in the continuum and Fano resonances in the strong mode coupling regime. *Advanced Photonics* **2019**, *1*, 016001.

- (13) Koshelev, K.; Bogdanov, A.; Kivshar, Y. Meta-optics and bound states in the continuum. *Science Bulletin* **2019**, *64*, 836–842. Special Topic: Electromagnetic Metasurfaces: from Concept to Applications
- (14) Yang, Y.; Peng, C.; Liang, Y.; Li, Z.; Noda, S. Analytical Perspective for Bound States in the Continuum in Photonic Crystal Slabs. *Phys. Rev. Lett.* **2014**, *113*, 037401.
- (15) Gansch, R.; Kalchmair, S.; Genevet, P.; Zederbauer, T.; Detz, H.; Andrews, A. M.; Schrenk, W.; Capasso, F.; Lončar, M.; Strasser, G. Measurement of bound states in the continuum by a detector embedded in a photonic crystal. *Light: Science & Applications* **2016**, *5*, e16147–e16147.
- (16) Yang, Y.; Jung, W.; Hur, C.; Kim, H.; Shin, J.; Choi, M.; Rho, J. Angle-Resolved Polarimetry with Quasi-Bound States in the Continuum Plasmonic Metamaterials via 3D Aerosol Nanoprinting. *ACS Nano* **2024**, *18*, 12771–12780.
- (17) Liang, Y.; Koshelev, K.; Zhang, F.; Lin, H.; Lin, S.; Wu, J.; Jia, B.; Kivshar, Y. Bound States in the Continuum in Anisotropic Plasmonic Metasurfaces. *Nano Lett.* **2020**, *20*, *6351–6356*.
- (18) Aigner, A.; Tittl, A.; Wang, J.; Weber, T.; Kivshar, Y.; Maier, S. A.; Ren, H. Plasmonic bound states in the continuum to tailor lightmatter coupling. *Science Advances* **2022**, *8*, eadd4816.
- (19) Joseph, S.; Sarkar, S.; Khan, S.; Joseph, J. Exploring the Optical Bound State in the Continuum in a Dielectric Grating Coupled Plasmonic Hybrid System. *Advanced Optical Materials* **2021**, *9*, 2001895.
- (20) Son, H.; Choi, T.; Kim, K.; Kim, Y.; Bang, J.; Kim, S.-J.; Lee, B.; Jeong, Y. Strong Coupling Induced Bound States in the Continuum in a Hybrid Metal-Dielectric Bilayer Nanograting Resonator. *ACS Photonics* **2024**, *11*, 3221–3231.
- (21) Wu, F.; Wu, J.; Guo, Z.; Jiang, H.; Sun, Y.; Li, Y.; Ren, J.; Chen, H. Giant Enhancement of the Goos-Hänchen Shift Assisted by Quasibound States in the Continuum. *Phys. Rev. Appl.* **2019**, *12*, 014028.
- (22) Wu, F.; Liu, D.; Xiao, S. Bandwidth-tunable near-infrared perfect absorption of graphene in a compound grating waveguide structure supporting quasi-bound states in the continuum. *Opt. Express* **2021**, *29*, 41975–41989.
- (23) Jeon, D.; Rho, J. Quasi-Trapped Guided Mode in a Metasurface Waveguide for Independent Control of Multiple Nonlocal Modes. *ACS Photonics* **2024**, *11*, 703–713.
- (24) Koshelev, K.; Kruk, S.; Melik-Gaykazyan, E.; Choi, J.-H.; Bogdanov, A.; Park, H.-G.; Kivshar, Y. Subwavelength dielectric resonators for nonlinear nanophotonics. *Science* **2020**, *367*, 288–292.
- (25) Koshelev, K.; Tang, Y.; Li, K.; Choi, D.-Y.; Li, G.; Kivshar, Y. Nonlinear Metasurfaces Governed by Bound States in the Continuum. *ACS Photonics* **2019**, *6*, 1639–1644.
- (26) Chen, Y.; Zhao, C.; Zhang, Y.; Qiu, C.-w. Integrated Molar Chiral Sensing Based on High-Q Metasurface. *Nano Lett.* **2020**, *20*, 8696–8703.
- (27) Gorkunov, M. V.; Antonov, A. A.; Kivshar, Y. S. Metasurfaces with Maximum Chirality Empowered by Bound States in the Continuum. *Phys. Rev. Lett.* **2020**, *125*, 093903.
- (28) Romano, S.; Zito, G.; Torino, S.; Calafiore, G.; Penzo, E.; Coppola, G.; Cabrini, S.; Rendina, I.; Mocella, V. Label-free sensing of ultralow-weight molecules with all-dielectric metasurfaces supporting bound states in the continuum. *Photon. Res.* **2018**, *6*, 726–733.
- (29) Romano, S.; Mangini, M.; Penzo, E.; Cabrini, S.; De Luca, A. C.; Rendina, I.; Mocella, V.; Zito, G. Ultrasensitive Surface Refractive Index Imaging Based on Quasi-Bound States in the Continuum. *ACS Nano* **2020**, *14*, 15417–15427.
- (30) Yang, Y.; Massuda, A.; Roques-Carmes, C.; Kooi, S. E.; Christensen, T.; Johnson, S. G.; Joannopoulos, J. D.; Miller, O. D.; Kaminer, I.; Soljačić, M. Maximal spontaneous photon emission and energy loss from free electrons. *Nat. Phys.* **2018**, *14*, 894–899.
- (31) Son, C.; Sultanov, V.; Santiago-Cruz, T.; Anthur, A. P.; Zhang, H.; Paniagua-Dominguez, R.; Krivitsky, L.; Kuznetsov, A. I.; Chekhova, M. V. Photon pairs bi-directionally emitted from a resonant metasurface. *Nanoscale* **2023**, *15*, 2567–2572.

- (32) Wang, M.; Li, H.; Xu, T.; Li, G.; Yu, M.; Jiang, B.; Xu, J.; Wu, J. Probing a chiral drug using long period fiber gratings. *Opt. Express* **2019**, 27, 31407–31417.
- (33) Ma, S.; Ahn, J.; Moon, J. Chiral Perovskites for Next-Generation Photonics: From Chirality Transfer to Chiroptical Activity. *Adv. Mater.* **2021**, *33*, 2005760.
- (34) Yan, B. Structural Chirality and Electronic Chirality in Quantum Materials. *Annu. Rev. Mater. Res.* **2024**, *54*, 97–115.
- (35) Jia, S.; Tao, T.; Xie, Y.; Yu, L.; Kang, X.; Zhang, Y.; Tang, W.; Gong, J. Chirality Supramolecular Systems: Helical Assemblies, Structure Designs, and Functions. *Small* **2024**, *20*, 2307874.
- (36) Sun, M.; Wang, X.; Guo, X.; Xu, L.; Kuang, H.; Xu, C. Chirality at nanoscale for bioscience. *Chem. Sci.* **2022**, *13*, 3069–3081.
- (37) Wang, Y.; Tay, A. Advances in Enantiomer-Dependent Nanotherapeutics. ACS Nano 2023, 17, 9850–9869.
- (38) Ceramella, J.; Iacopetta, D.; Franchini, A.; De Luca, M.; Saturnino, C.; Andreu, I.; Sinicropi, M. S.; Catalano, A. A Look at the Importance of Chirality in Drug Activity: Some Significative Examples. *Applied Sciences* **2022**, *12*, 10909.
- (39) McVicker, R. U.; O'Boyle, N. M. Chirality of New Drug Approvals (2013–2022): Trends and Perspectives. *J. Med. Chem.* **2024**, *67*, 2305–2320.
- (40) Kim, J.; Rana, A. S.; Kim, Y.; Kim, I.; Badloe, T.; Zubair, M.; Mehmood, M. Q.; Rho, J. Chiroptical Metasurfaces: Principles, Classification, and Applications. *Sensors* **2021**, *21*, 4381.
- (41) Khaliq, H. S.; Nauman, A.; Lee, J.-W.; Kim, H.-R. Recent Progress on Plasmonic and Dielectric Chiral Metasurfaces: Fundamentals, Design Strategies, and Implementation. Advanced. *Opt. Mater.* **2023**, *11*, 2300644.
- (42) Mun, J.; Kim, M.; Yang, Y.; Badloe, T.; Ni, J.; Chen, Y.; Qiu, C.-W.; Rho, J. Electromagnetic chirality: from fundamentals to nontraditional chiroptical phenomena. *Light: Science & Applications* **2020**, *9*, 139.
- (43) Spreyer, F.; Mun, J.; Kim, H.; Kim, R. M.; Nam, K. T.; Rho, J.; Zentgraf, T. Second Harmonic Optical Circular Dichroism of Plasmonic Chiral Helicoid-III Nanoparticles. *ACS Photonics* **2022**, *9*, 784–792.
- (44) Kakkar, T.; Keijzer, C.; Rodier, M.; Bukharova, T.; Taliansky, M.; Love, A. J.; Milner, J. J.; Karimullah, A. S.; Barron, L. D.; Gadegaard, N.; Lapthorn, A. J.; Kadodwala, M.; et al. Superchiral near fields detect virus structure. *Light: Science & Applications* **2020**, *9*, 195.
- (45) Kim, Y.; Kim, H.; Yang, Y.; Badloe, T.; Jeon, N.; Rho, J. Three-dimensional artificial chirality towards low-cost and ultra-sensitive enantioselective sensing. *Nanoscale* **2022**, *14*, 3720–3730.
- (46) Mao, L.; Cheng, P.; Liu, K.; Lian, M.; Cao, T. Sieving nanometer enantiomers using bound states in the continuum from the metasurface. *Nanoscale Adv.* **2022**, *4*, 1617–1625.
- (47) Lee, Y. H.; Won, Y.; Mun, J.; Lee, S.; Kim, Y.; Yeom, B.; Dou, L.; Rho, J.; Oh, J. H. Hierarchically manufactured chiral plasmonic nanostructures with gigantic chirality for polarized emission and information encryption. *Nat. Commun.* 2023, 14, 7298.
- (48) Huang, Z.; Wang, J.; Jia, W.; Zhang, S.; Zhou, C. Controllable perfect chiral optical response in planar metasurfaces empowered by quasi-bound states in the continuum. *Opt. Express* **2024**, *32*, 33029–33041.
- (49) Shi, T.; Deng, Z.-L.; Geng, G.; Zeng, X.; Zeng, Y.; Hu, G.; Overvig, A.; Li, J.; Qiu, C.-W.; Alu, A.; Kivshar, Y. S.; Li, X.; et al. Planar chiral metasurfaces with maximal and tunable chiroptical response driven by bound states in the continuum. *Nat. Commun.* 2022, 13, 4111.
- (50) Chen, Y.; Deng, H.; Sha, X.; Chen, W.; Wang, R.; Chen, Y.-H.; Wu, D.; Chu, J.; Kivshar, Y. S.; Xiao, S.; et al. Observation of intrinsic chiral bound states in the continuum. *Nature* **2023**, *613*, 474–478.
- (51) Dixon, J.; Lawrence, M.; Barton, D. R.; Dionne, J. Self-Isolated Raman Lasing with a Chiral Dielectric Metasurface. *Phys. Rev. Lett.* **2021**, *126*, 123201.
- (52) Lv, S.; Hu, F.; Luo, W.; Xu, H.; An, L. Design of tunable selective light-absorbing metasurfaces driven by intrinsically chiral

- quasi-bound states in the continuum. Opt. Express 2024, 32, 30053-30064.
- (53) Kühner, L.; Wendisch, F. J.; Antonov, A. A.; Bürger, J.; Hüttenhofer, L.; de S. Menezes, L.; Maier, S. A.; Gorkunov, M. V.; Kivshar, Y.; Tittl, A. Unlocking the out-of-plane dimension for photonic bound states in the continuum to achieve maximum optical chirality. Light: Science & Applications 2023, 12, 250.
- (54) Zhang, D.; Liu, T.; Lei, L.; Deng, W.; Wang, T.; Liao, Q.; Liu, W.; Xiao, S.; Yu, T. Tailoring intrinsic chirality in a two-dimensional planar waveguide grating via quasibound states in the continuum. *Phys. Rev. B* **2024**, *109*, 205403.
- (55) Salzberg, C. D.; Villa, J. J. Infrared Refractive Indexes of Silicon Germanium and Modified Selenium Glass*. *J. Opt. Soc. Am.* 1957, 47, 244–246.
- (56) Gurvitz, E. A.; Ladutenko, K. S.; Dergachev, P. A.; Evlyukhin, A. B.; Miroshnichenko, A. E.; Shalin, A. S. The high-order toroidal moments and anapole states in all-dielectric photonics. *Laser & Photonics Reviews* **2019**, *13*, 1800266.
- (57) Lepetit, T.; Kanté, B. Controlling multipolar radiation with symmetries for electromagnetic bound states in the continuum. *Phys. Rev. B* **2014**, *90*, 241103.
- (58) Koshelev, K.; Lepeshov, S.; Liu, M.; Bogdanov, A.; Kivshar, Y. Asymmetric metasurfaces with high-Q resonances governed by bound states in the continuum. *Physical review letters* **2018**, *121*, 193903.
- (59) Sharma, S.; Lahiri, B.; Varshney, S. K. Accidental BIC in All-Dielectric Nano-Sized Tri-Air holes Silicon Disk Resonator. *Conference on Lasers and Electro-Optics: Applications and Technology* **2022**, DOI: 10.1364/CLEO AT.2022.JTu3A.68.
- (60) Hsu, C. W.; Zhen, B.; Lee, J.; Chua, S.-L.; Johnson, S. G.; Joannopoulos, J. D.; Soljačić, M. Observation of trapped light within the radiation continuum. *Nature* **2013**, *499*, 188–191.
- (61) Sadrieva, Z.; Frizyuk, K.; Petrov, M.; Kivshar, Y.; Bogdanov, A. Multipolar origin of bound states in the continuum. *Phys. Rev. B* **2019**, *100*, 115303.
- (62) Sadrieva, Z. F.; Sinev, I. S.; Koshelev, K. L.; Samusev, A.; Iorsh, I. V.; Takayama, O.; Malureanu, R.; Bogdanov, A. A.; Lavrinenko, A. V. Transition from Optical Bound States in the Continuum to Leaky Resonances: Role of Substrate and Roughness. *ACS Photonics* **2017**, *4*, 723–727.
- (63) Singh, R.; Al-Naib, I. A. I.; Yang, Y.; Roy Chowdhury, D.; Cao, W.; Rockstuhl, C.; Ozaki, T.; Morandotti, R.; Zhang, W. Observing metamaterial induced transparency in individual Fano resonators with broken symmetry. *Appl. Phys. Lett.* **2011**, *99*, 201107.
- (64) Cong, L.; Singh, R. Symmetry-protected dual bound states in the continuum in metamaterials. *Advanced Optical Materials* **2019**, *7*, 1900383.
- (65) Wu, J.; Xu, X.; Su, X.; Zhao, S.; Wu, C.; Sun, Y.; Li, Y.; Wu, F.; Guo, Z.; Jiang, H.; Chen, H. Observation of Giant Extrinsic Chirality Empowered by Quasi-Bound States in the Continuum. *Phys. Rev. Appl.* **2021**, *16*, 064018.
- (66) Gorkunov, M. V.; Antonov, A. A.; Tuz, V. R.; Kupriianov, A. S.; Kivshar, Y. S. Bound States in the Continuum Underpin Near-Lossless Maximum Chirality in Dielectric Metasurfaces. *Advanced Optical Materials* **2021**, *9*, 2100797.